Impact Vaporization as a Possible Source of Mercury's Calcium Exosphere

Rosemary M. Killen, NASA Goddard Space Flight Center, Greenbelt, Maryland, USA
Joseph M. Hahn, Space Science Institute, c/o Center for Space Research, University of Texas at Austin, 3925 West Braker Lane, Suite 200, Austin, TX 78759-5378, USA;
jhahn@spacescience.org

Corresponding Author: R.M. Killen, Code 695, NASA Goddard Space Flight Center, Greenbelt, Maryland, 20771, USA. (rosemary.killen@nasa.gov); 301-286-6574

Highlights

- We show that Mercury's calcium exosphere, which is observed to vary seasonally about that planet's orbit, can be attributed to impact vaporization by interplanetary dust.
- A comparison of models to MESSENGER observations shows that the seasonal variations in that Ca signal result from the planet's sizable orbital eccentricity and inclination which cause that planet to experience significant radial and vertical excursions through the interplanetary dust cloud.
- The model developed here also requires an additional source localized at 25±5° degrees after Mercury's perihelion, and that may be due to a meteor stream possibly associated with the nearby comet Encke.
- Impact vaporization can explain the source rate and true anomaly angle variations in the calcium exosphere but an additional mechanism must be invoked to explain the extreme temperature.

Abstract

Mercury's calcium exosphere varies in a periodic way with that planet's true anomaly. We show that this pattern can be explained by impact vaporization from interplanetary dust with variations being due to Mercury's radial and vertical excursions through an interplanetary dust disk having an inclination within 5 degrees of the plane of Mercury's orbit. Both a highly inclined dust disk and a two-disk model (where the two disks have a mutual inclination) fail to reproduce the observed variation in calcium exospheric abundance with Mercury true anomaly angle. However, an additional source of impacting dust beyond the nominal dust disk is required near Mercury's true anomaly (ν) 25° ±5°. This is close to but not coincident with Mercury's true anomaly (ν=45°) when it crosses comet 2P/Encke's present day orbital plane. Interestingly, the Taurid meteor storms at Earth, which are also due to Comet Encke, are observed to occur when Earth's true anomaly is ±20 or so degrees before and after the position where Earth and Encke orbital planes cross. The lack of exact correspondence with the present day orbit of Encke may indicate the width of the potential stream along Mercury's orbit or a previous cometary orbit. The extreme energy of the escaping calcium, estimated to have a temperature >50000 K if the source is thermal, cannot be due to the impact process itself but must be imparted by an additional mechanism such as dissociation of a calcium-bearing molecule or ionization followed by recombination.

Keywords:
Mercury, Atmosphere
Interplanetary Dust
Impact processes

1. Introduction

Mercury is surrounded by a surface-bounded exosphere with seven known components: H, He, O, Na, K, Ca and Mg. Calcium has been observed in Mercury's exosphere for over a decade, having been discovered by Bida et al. (2000) using the Keck telescope on Mauna Kea. The Mercury Atmospheric and Surface Composition Spectrometer (MASCS) instrument, a UV-visible spectrometer on the MErcury Surface, Space ENvironment, GEochemistry, and Ranging (MESSENGER) spacecraft (McClintock and Lankton, 2007) has been taking spectroscopic measurements of neutral atoms and one ion (Ca^+) in Mercury's exosphere since the first flyby of MESSENGER with Mercury in January, 2008. Limb scan observations

of the Ca exosphere of Mercury were analyzed in Burger et al., 2012 and 2014. They show a repeatable seasonal pattern in total source rate with respect to Mercury true anomaly angle, ν (Burger et al., 2014). (The true anomaly is the planet's angular coordinate measured from the direction of perihelion in the orbital plane.) In this paper we attempt to model the seasonal variations in the impact vaporization rate of calcium from Mercury's surface due to the influx of interplanetary dust. To explain a persistent enhancement at true anomaly angle 25°±5°, we also consider impact vaporization due to a meteor stream, possibly resulting from comet Encke whose orbit lies quite close to Mercury.

In the following sections we first present the Ca observations obtained by MESSENGER's MASCS ultraviolet spectrometer (Section 2), then in Section 3 we discuss the models of the interplanetary dust disk that we will use (3.1), and finally we discuss our impact vaporization model (Section 3.2). In section 4 we discuss the results. The effect of varying the inclination of the dust disk is discussed in 4.1, and then we introduce the effect of a possible meteor shower in 4.2. The discussion follows in Section 5; we briefly compare our results with previous work in section 5.1; then we discuss possible modes of energization of the neutral calcium in section 5.2, and finally in section 5.3 we discuss the fraction of impact vapor escaping at extreme temperature. Section 6 contains conclusions.

2. Observations

Observations from the MESSENGER MASCS spectrometer show that the calcium exosphere is concentrated on the dawn hemisphere with a very wide distribution in local time. Data obtained by the MESSENGER MASCS spectrometer during more than 8 Mercury years (March 18, 2011 - March 17, 2013) were analyzed and published by Burger et al. (2014). Figure 1, derived from MESSENGER MASCS observations by Burger et al. (2014), shows the total source rate of Ca atoms into the exosphere over the whole planet in atoms s^{-1} derived from fits of MASCS data to the output of a Monte Carlo exosphere code. The source rate is remarkably repeatable over the orbital period of Mercury. The most intriguing part of this figure is the peak at true anomaly ν=25°±5°; one might expect the peak to occur at perihelion, ν=0°, because interplanetary dust is concentrated sunward.

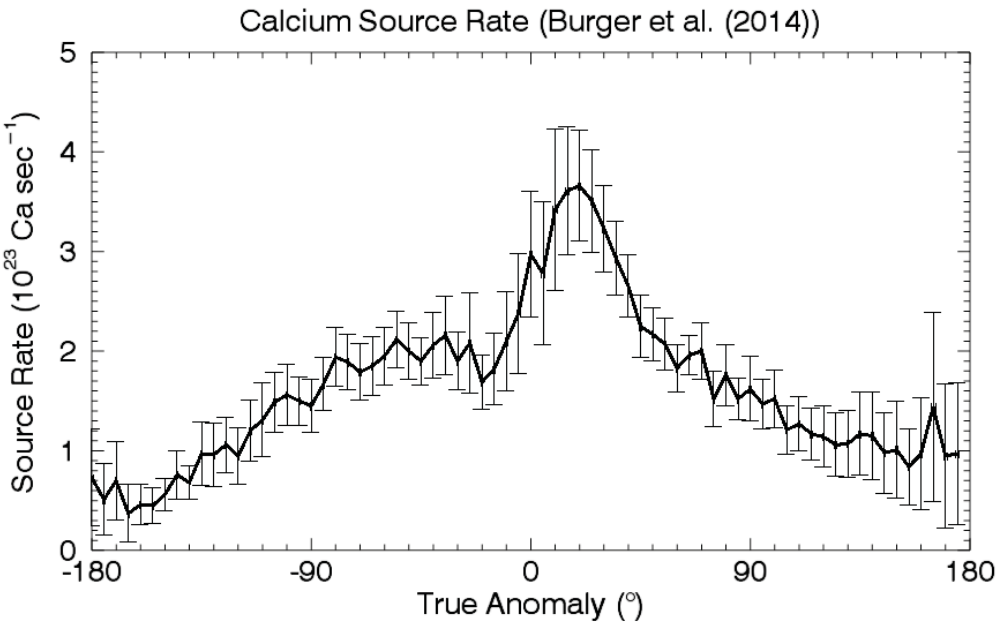

Figure 1. The total planetary calcium source rate into Mercury's exosphere is a periodic function of Mercury true anomaly, ν. Mercury is at perihelion when the true anomaly is 0° and at aphelion when the true anomaly is ±180°. The black curve is the total calcium source rate summed over the planet at each true anomaly angle, derived from observations obtained by the MESSENGER MASCS spectrometer March 2011 - March 2013 (plot adapted from Burger et al., 2014).

In addition to a true anomaly angle variation there is a marked dawn/dusk asymmetry in the calcium exosphere (Burger et al., 2014). We know that the flux of large meteoroids at Earth has been shown to be asymmetric with respect to the morning and evening hemispheres and to depend on the position of the planet along its orbit and on the particle size (e.g. Fentzke and Janches, 2008; Janches et al., 2006), and we expect the same to be true at Mercury. The ratio of impacts on morning to evening on Mercury's surface was derived by Marchi et al. (2005) to be about 1.2 - 1.5 at perihelion and about 0.8 - 1 at aphelion. Given that the column abundance of Ca, N, is on the order of $1x10^{9}$ cm^{-2}, and the derived e-folding distance, H, is about $4x10^{8}$ cm, the maximum number density of Ca at the morning terminator, N/H, is only about 3 cm^{-3}, and a 3/2 asymmetry would imply a density at the evening terminator of <2 cm^{-3}. The MASCS sensitivity is such that a column density of $<1.5x10^{8}$ would be undetectable. The Burger (2014) model does a good job of fitting the observed spatial pattern in the exospheric abundance with a dawn source because of redistribution of vapor in the exosphere.

The following section provides an explanation for the seasonal variation in the abundance of Mercury's exospheric Ca. In subsequent sections we address other observations that are not yet completely understood, including the Ca component's extreme temperature.

3. Models

3.1 Model of the dust disk

We seek to determine whether the observed variation with true anomaly angle, ν, observed in Mercury's Ca exosphere can be explained by impact vaporization by interplanetary dust. To that end we have modeled the impact vaporization rate at Mercury as a function of Mercury's position in the interplanetary dust cloud.

The cloud of interplanetary dust in the inner heliosphere is disk-like, with its dust concentrated in a plane that lies near the ecliptic. To model the dust flux onto Mercury, we employed a dust-disk model derived by Hahn et al. (2002), fitted to optical observations of dust whose heliocentric orbits are also in the vicinity of Mercury and Venus. In brief, this model assumes three dust sources, denoted by subscript j: 1) asteroids and Jupiter-family comets, 2) Halley type comets, and 3) Oort cloud comets and interstellar sources, respectively.

The spatial distribution of interplanetary dust is written as the sum over several components, one being an isotropic source from the Oort cloud comets, and the other two having inclination distributions that are Gaussian. The inclination distributions are taken from Hahn et al., 2002, section 4.2.1, which can be consulted for further details. Each source has a unique inclination distribution $g_j(i)$ with respect to the dust disk midplane:

$$g_j(i) = \frac{2}{\pi} \sin(i) \times \begin{cases} 1, & \text{j=iso} \\ c_j e^{-(i/\sigma_j)^2/2}, & \text{otherwise} \end{cases} \qquad (1)$$

where $g_j(i)$ is the fractional abundance of population j's dust that has inclination i. Each source population j produces dust that has a latitude distribution, $h_j(\beta)$, that is:

$$h_j(\beta) = \int_{\beta}^{\pi/2} \frac{g_j(i)di}{\sqrt{\sin^2 i - \sin^2 \beta}}$$

. (2)

In other words, each dust particle is in orbit with a particular inclination, i, with respect to the dust disk's mid-plane, and these inclinations are integrated to obtain the dust density at a particular latitude, β. Here the dust density is assumed to vary as

$$n(R,\beta) \propto R^{-\chi_j} h_j(\beta) \ , \quad (3)$$

where R is the polar radial coordinate from the Sun, so this factor accounts for radial changes in dust density of population j's dust at latitude β above/below the dust disk's midplane, which itself is likely to be tipped no more than a few degrees from the ecliptic plane (Figs 5 and 12 of Hahn et al., 2002).

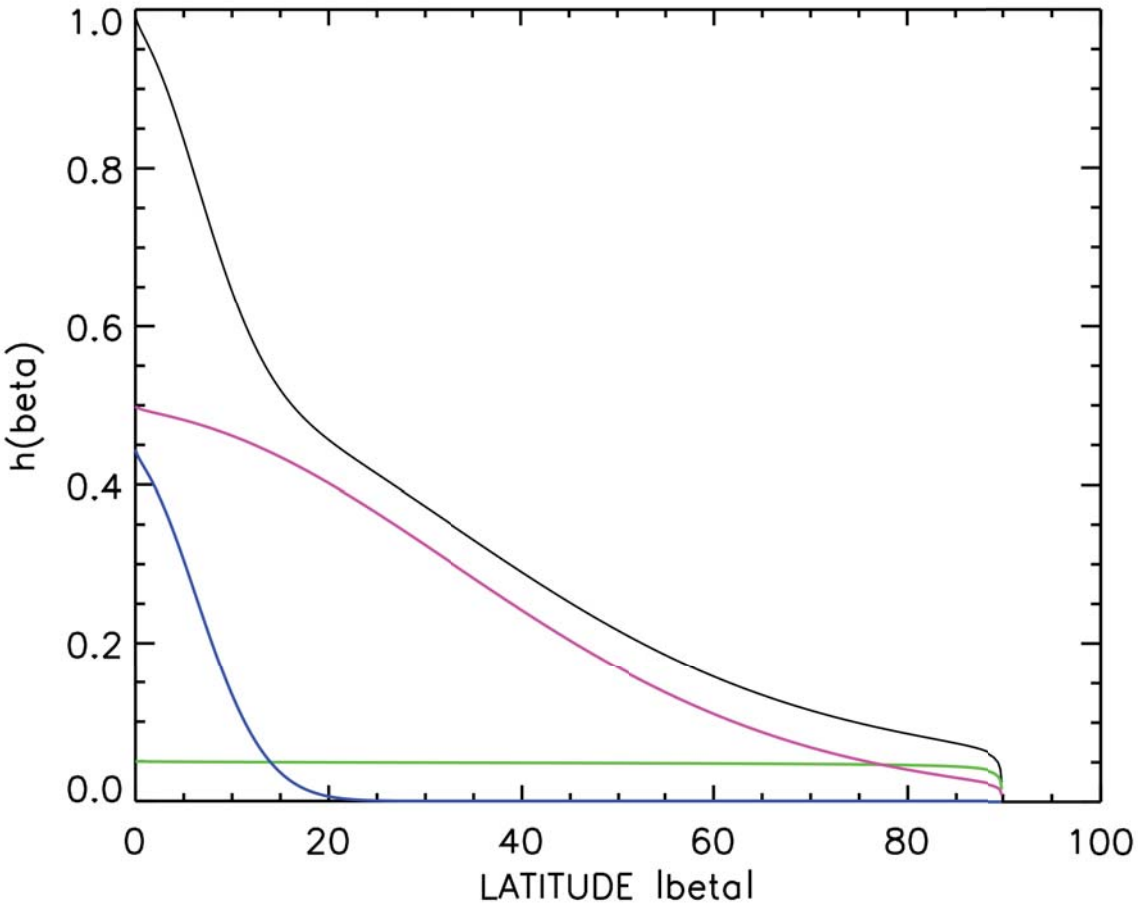

Figure 2. h(β) (black curve) is the abundance of dust at latitude β relative to that in the dust-disk's midplane at β=0 (Hahn et al., 2002), with β related to the cylindrical coordinates R, z, via tan(β)=z/R. The three populations of interplanetary dust are: lower inclination dust generated by colliding asteroids and outgassing Jupiter family comets (blue), higher inclination dust generated by Halley type comets (magenta), and isotropic dust produced by Oort cloud comets (green).

Each population's density varies in heliocentric distance with a distinct power law $\propto R^{-\chi_j}$. The three populations are: dust from asteroids and Jupiter family comets having characteristic inclinations $sigma_j$=7° (low); dust from Halley-type comets with typical inclinations $sigma_j$=33° (extended); and an isotropic source from Oort cloud comets whose inclination distributions are uniform thus g_j=1 in Equation 2. The populations are also weighted by a factor f_j that provides the relative weight of the dust population j and χ is the radial dependence of that population (see Table 1).

Table 1. Nominal parameters of the 3 populations of interplanetary dust.

Population	f_j	χ_j
low	0.45	1.00
high	0.50	1.45
isotropic	0.05	2.00

The vaporization of dust that is impacting Mercury will depend on the dust density and its relative speed, both of which vary with that planet's true anomaly ν. The relative orientations of the dust disk to the orbit of Mercury will affect the dust flux to the surface, so these results will be sensitive to the inclination of the dust-disk relative to Mercury's orbital plane, as well as to the dust disk's longitude of the ascending node Omega, which in this study will be measured in Mercury's orbital plane from Mercury's longitude of perihelion (i.e. when Mercury is at ν=0 in Figure 1).

The most uncertain elements of the dust disk model are the tilt of the dust disk's midplane relative to Mercury's orbital plane and the orientation of the disk's midplane. That tilt and orientation of the dust disk can be described by an inclination, i, that is probably no more than a few degrees from the ecliptic (see Figs 5 and 12 of Hahn et al., 2002), and by the longitude of the ascending node, Ω, which is the ecliptic longitude where the dust-disk's mid-plane crosses the ecliptic plane. Estimates of Ω range from Ω=87°±4 (Leinert et al., 1980; Helios data); 77.7°±0.6 (DIRBE model); 66° (Leinert et al., 1976), to 53° (Reach, 1991). In our models, in order to

192 determine the best fit to the seasonal variation in the Ca source rate, we varied the inclination of
193 the dust disk, the dust disk's longitude of ascending node, and also the radial power, χ, of the low
194 population dust.
195
196 **3.2. Impact Vaporization Model**
197
198 We have used the impact vaporization model previously described in Morgan and Killen (1998)
199 and in Killen et al. (2005). This model is based on the planar impact approximation (Melosh,
200 1989) with parameters from Melosh (1989) and Lange and Ahrens (1982). The equations are
201 given in Killen et al. (2005) Appendix I. The density of the impacting interplanetary dust was
202 computed using the Hahn et al. (2002) model, with dust impact velocity drawn from the velocity
203 distribution of Cintala (1992), equation (A11a). The dust-density variation with heliocentric
204 distance is already included in the Hahn formalism, so we used Cintala's Eqn (A11a) rather than
205 (A11b). Gravitational focusing is accounted for in the Cintala (1992) formalism. The dust impact
206 model used here accounts for variation in the impacting dust flux that is due to Mercury's radial
207 and vertical motion through the interplanetary cloud that are a result of Mercury's substantial
208 eccentricity and inclinations. The dust flux at Mercury is scaled from that at Earth using equation
209 A11a of Cintala (1992) assuming the Love and Brownlee (1993) accretion rate of cosmic dust at
210 the Earth is $4\pm2\text{x}10^7$ kg/yr. Our formalism accounts for gravitational focusing by Mercury.
211
212 The vaporization rate is calculated as a function of the impacting dust velocity and is integrated
213 over the velocity function (Killen et al., 2005; Appendix I), which has a median impact speed of
214 20 km/s at Mercury (Cintala, 1992). According to Collette et al. (2014) the impact vaporization
215 as a percent of projectile mass is about 40% at an impact velocity of 20 km/s (the highest impact
216 velocities they reported), which is consistent with the O'Keefe and Ahrens (1977) condition that
217 we use, namely that significant vaporization commences at $v_i/v_{sound}=3.1$, where v_i is the impact
218 velocity and v_{sound} is the velocity of sound in the target. The velocity of sound in rock forming
219 silicate materials is 5 - 8 km/s, so the onset of significant vaporization is 16 - 25 km/s. Our
220 impact vaporization rate $f_v(v_i)$ is scaled to

221 $$f_v(v_i) = \frac{\rho_m}{\rho_t}\{\frac{v_i}{v_{sound}}\}^2, \qquad (4)$$

222
223 where ρ_m is the density of the meteoroid, ρ_t is the density of the target. Additional model
224 parameters are reported in Table 3 and the meaning of quantities such as ctype, mtype, and itype
225 are detailed in Killen et al. (2005). Basically they are set to choose the type of impactor and
226 target. In particular, the target material here is assumed to be regolith whose thermodynamic

constants are from Cintala (1992). The projectile dust grain is assumed to be a carbonate meteoroid and the constant C in Table 3 is related to the bulk speed of sound while dimensionless constant S is obtained from shock-wave experiments. That quantity enters into the linear shock-particle velocity equation of state. Because we do not have all physical quantities for "regolith" other target quantities (having subscript t) assume the target is basalt while the projectile quantities (subscript p) assume calcite (see Melosh, 1989, page 232).

Given that more than half of the micrometeoritic flux is impacting Mercury at velocities greater than 20 km/s (Cintala 1992), significant vaporization is expected. In fact, our result may be an underestimate because the velocity distribution at Mercury calculated by Marchi et al. (2005) was double-peaked, with a second peak at about 40 km/s. Marchi et al. (2005) report a mean impact velocity for all of their distributions of about 30 km s^{-1}, but with double peaks (one at 30 km/s and one at 40 km/s) and with tails spanning from about 15 to 80 km s^{-1}. Thus the Marchi et al. (2005) velocity distribution at Mercury is shifted to higher impact velocities by about 20 km/s from the one we use. However, their velocity distribution only applies to meteoroids coming from the Main Belt, and not dust in general. We tested the effect of increasing the mean impact velocity to 35 km/s, but because mass density and velocity both affect the flux, in our model the higher velocity stream simply requires a lower dust density. We cannot simultaneously constrain dust density and velocity without a constraint on one or the other. The velocity distribution derived by Borin et al. (2009) for small particles (radius of 5 μm and 100 μm) has a slightly lower mean velocity than that of Cintala (1992) and a much less extended high velocity tail. We conclude that the Cintala distribution (in between the Borin et al. and the Marchi et al. results) is probably reasonable for small particles, which make up the more or less constant background, as opposed to large meteors that are sporadic and widely distributed in frequency. The highly repeatable seasonal pattern in the exosphere cannot be attributed to sporadic meteors.

Although the porosity of Mercury's regolith is high, we have assumed zero porosity in these calculations because our code does not compensate for sticking of atoms to regolith grains on multiple encounters with soil. Higher porosity will increase the derived vaporization rate by up to a factor of ~5. However, only about one third of this will escape the regolith due to interactions with the soil (Cassidy and Johnson, 2005). The assumption of zero porosity compensates for lack of a more detailed treatment of multiple scattering, and it gives a conservative estimate of vapor that escapes into the exosphere. Another, possibly greater, source of uncertainty is the amount of impact vapor that remains in the uncondensed state after the initial fireball becomes collisionless (e.g. Berezhnoy and Klumov, 2008). Our code gives the total vapor phase (as opposed to melt plus vapor) and we assume that the calcium is released in

the molecular state. We assumed 3.5% (±0.7)% Ca in the regolith by number (Evans et al., 2012). Both the regolith and impacting dust contribute to the vapor. We assume that the impacting dust and the regolith have the same Ca fraction. Because this is a global average calculation, we have not considered spatial variations in the Ca abundance in the Mercury soil. However, we note that a spatially asymmetric Ca abundance in the soil would produce a bi-annual variation due to the spin-orbit coupling of the planet's motion, not the annual variation that is seen. The low abundance of Ca in the lunar and Mercurian exospheres is explained by the condensation of Ca into dust grains during expansion of the cooling impact-produced vapor cloud (Berezhnoy, 2010).

The fraction of uncondensed atomic Ca that is observed at high altitude by the MASCS instrument is a free parameter in our model and is scaled to match the data: it is generally less than 10% as discussed in section 4. This fraction varies slightly for different assumptions, and is most sensitive to the radial dependence of the dust density, which we varied. The remaining thermodynamic constants used in the impact vapor code are also given in Table 3.

Table 3. Thermodynamic Constants and Surface/Projectile Constants used

parameter	value	Comments
ρtarget (Kg/m^3)	1800	
ρ impactor	1800	
fraction Ca	0.0354	
porosity	0.0	Gives a lower limit on impact vaporization rate
vesc (km/s)	4.25	Mercury escape velocity
mass number (AMU)	40	
radius target (km)	2340	
ctype	3	Hv=9.64E10; regolith
mtype	1	used to calculate the minimum velocity for vaporization; Al onto enstatite; aa=21.014, bb=-14.154, cc=3.058 vmin1=(aa+bb*m+cc*m^2); m=distention
itype	1	silicaceous impactor
C_t (km/s)	2.60	basalt target; Melosh, 1989; Table AII.2; Linear shock-particle velocity equation of state parameters; related to the bulk sound speed
S_t	1.62	basalt target; related to the Gruneisen parameter Γ
C_p (km/s)	3.80	carbonate projectile
S_p	1.42	carbonate projectile

4. Results

The following shows results from selected models that calculate the rate at which Mercury sweeps up interplanetary dust and produces Ca vapor via impacts. This rate varies seasonally due to Mercury's substantial radial and vertical motion through the circumsolar dust-disk. Section 4.1 will consider how the Ca production rate varies with the dust-disk's relative inclination, which controls how far Mercury travels from the dust-disk's midplane and thus alters the local dust density. Section 4.2 will show that an additional source of dust is needed of explain the Messenger observations, and it is suggested that the dust could be due to a meteor storm associated with the nearby comet Encke.

4.1 Effect of varying the inclination of a nominal dust disk

In Figure 3 we show the effect of varying the inclination of the dust disk from 45° to a low inclination dust disk of 5°. The impact vaporization rates shown in Figure 3 as a function of true anomaly angle, ν, vary as the planet traverses the modeled dust disk. The coordinate system used here and in Figures 4 and 7, is in the plane of Mercury's orbit so the dust disk's inclination, i, is measured relative to Mercury's orbital plane. This coordinate system's x axis is oriented towards Mercury's perhelion, and all longitudes will be measured from the x axis. Consequently the dust disk's longitude of ascending node, Ω, will also be Mercury's true anomaly, ν, when it passes through the dust-disk's midplane, which happens again at $\nu=\Omega \pm 180°$. For a low inclination disk, the maximum impact vaporization rate occurs at Mercury's perihelion because in this case the heliocentric radial excursion dominates the impactor flux variation. As the inclination increases, the maximum in source rate occurs where Mercury's orbital plane crosses the dust disk plane at the minimum heliocentric radial distance. But also note that a secondary peak occurs where the two planes cross again at the larger radial distance.

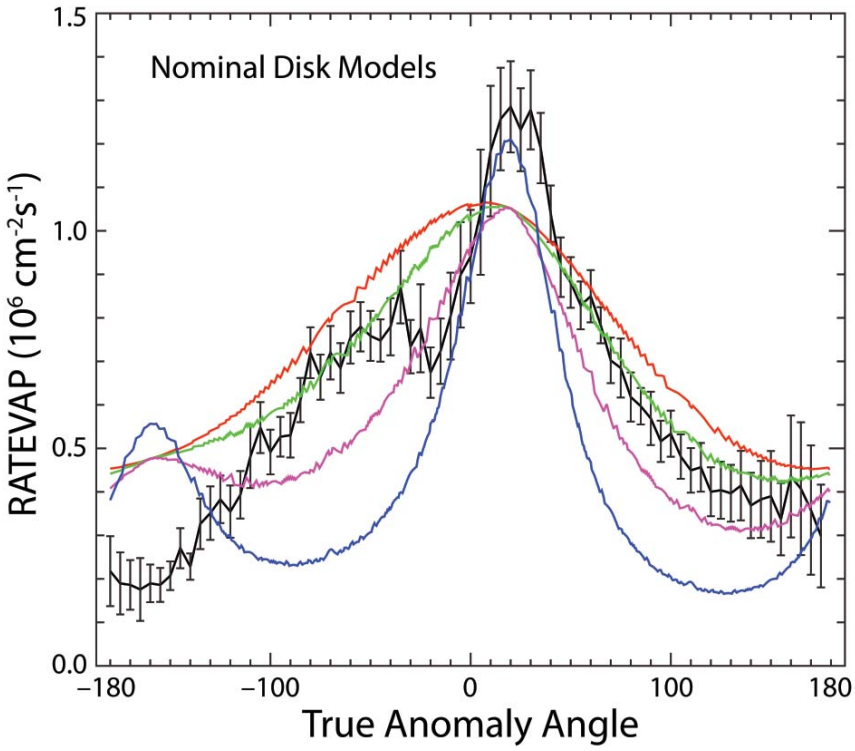

Figure 3. Ratevap is the rate at which atomic calcium is ejected into the exosphere. It is the fraction of the impact vaporization rate of Ca-bearing minerals in all forms, including molecular, that remains in the uncondensed state at the point when the vapor cloud becomes collisionless. We have plotted ratevap vs. ν for a dust disk with ascending node 20°. The figure shows how results are sensitive to the dust disk's inclination, i, and shows why a single disk model cannot account for the observed seasonal variations in exospheric Ca. Only the inclination relative to Mercury's orbital plane is different for each model: i=5 (red), i=10 (green), i=20 (magenta) and i=45 (blue) degrees, respectively. The fraction of Ca-bearing vapor that remains in the uncondensed state is set at 12% for all of these runs for comparison purposes. The vaporization rate is in units of 10^6 atoms cm^{-2} s^{-1}. The data are shown in black. None of these models can fit the data (black). To keep the parameters constant except inclination, we have not attempted a best-fit model here.

Although the increased Ca source rate at Mercury ν=25°±5° could in principle be caused by a highly inclined dust disk (e.g. blue line in Figures 3), an increased vapor rate would also occur near aphelion, ν =-160° where the two planes cross again. This is not seen in the data (black curve). This secondary peak would be due to Mercury passing through the dust-disk's midplane again but this time just after apoapse where the dust density is smaller than at periapse. Because this secondary peak is not seen in the data, shown in black, the inclination of the dust disk with respect to Mercury's orbital plane is constrained to be less than about 10° (green curve in Figure

3). But in this case there still remains an additional source that is unaccounted for. Observations of the zodiacal light show that the dust disk midplane is certainly no more than a few degrees away from the ecliptic plane (Hahn et al., 2002). Leinert et al. (1980) estimate that the dust-disk ecliptic inclination is i=3.3° ±0.4° with an ascending node Ω=77° ±10° while Misconi and Weinberg (1978) report i=2.7° with Ω=85°. Therefore the dust disk's mid-plane with respect to Mercury's orbital plane is probably between 3° and 10°. The final fraction of Ca-bearing vapor in the uncondensed atomic state is set at 12% of the total Ca-bearing vapor emitted in each of the simulations in Figure 3, chosen to most closely fit the observations. Note that a secondary peak in the simulations of Ca signal near ν=-160° (Fig. 3) could be avoided if the dust density falls off much more rapidly with heliocentric distance, R. However, a steep radial gradient in the dust disk is contrary to dust models based on the zodiacal light (e.g., Hahn et al., 2002), and can be rejected.

In Figure 4 we show a nominal low inclination disk (magenta) with a radial dependence r^{-2}, and a high inclination disk (green) with a radial dependence r^{-3}. Although the steep radial dependence of dust density minimizes the secondary impact vaporization peak, it does not eliminate the secondary peak at ν=-150°. Because this high inclination model (green) is calibrated to measurements at 1 AU, the fraction of total vapor that is seen in the uncondensed state for the r^{-3} model is only 0.02 (2%), much less than the fraction in Figure 3. The actual amount of vapor remaining in the atomic uncondensed state after the initial fireball becomes collisionless will be similar because it must be scaled to match the data.

So to summarize, none of the nominal dust disk models considered thus far provide an adequate fit to the data.

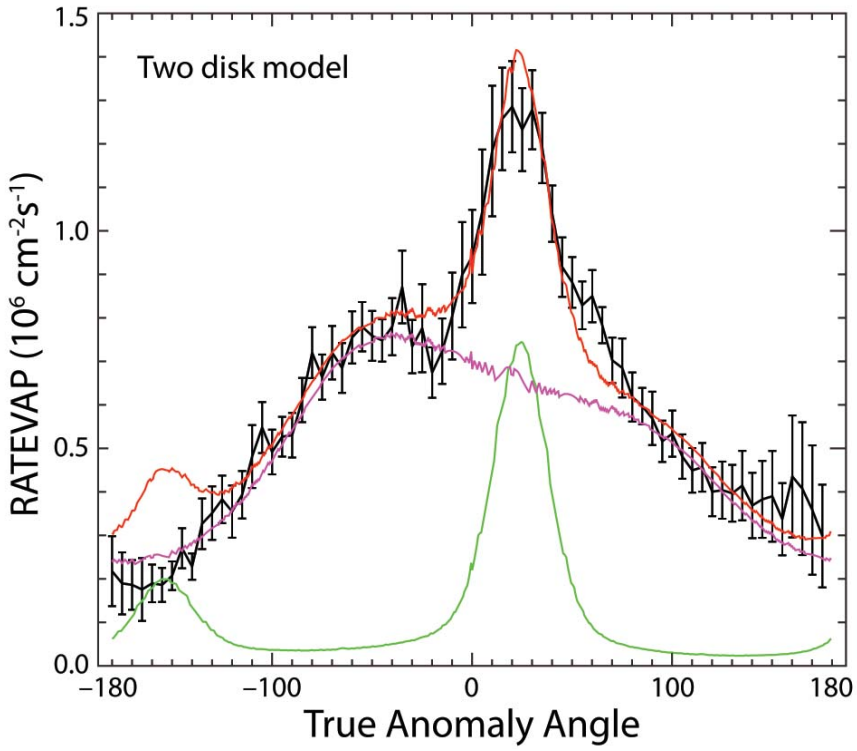

Figure 4. The impact vaporization rate of Ca vs. ν for two dust disks at a high relative inclination. The rate is in units of 10^6 atoms cm^{-2} s^{-1}. Dust disk 1 (magenta) has inclination 10° with respect to Mercury's orbital plane, ascending node 290°, radial dependence R^{-2}; dust disk 2 (green) has inclination 45°, ascending node 25°, and radial dependence R^{-3}, with the sum of the two disks plotted in red, and the data in black. We reject the steep radial dependence model.

4.2 Effect of a Meteor Stream

The enhancement in Ca source rate near true anomaly angle 25°±5° cannot be modeled by impact vaporization from a single dust disk (Figure 3) because such a disk would cause two enhancements in the vapor rate, one at each node where the two planes cross (once when Mercury's true anomaly equals the disk ascending node and then again when Mercury's true anomaly equals the disk ascending node plus 180°. For a similar reason we cannot find a satisfactory fit using an interplanetary dust model that is composed of two circumsolar dust disks (Figure 4). So for these reasons we now consider whether the observed Ca excess at nu= 25°±5° could be due to a meteor storm, which is a concentration of dust that is localized at or near a comet's orbit about the Sun. And in the following we focus on possible meteor storms from comet Encke, which is a short period comet that has produced

a dust trail all along its orbit (see Figure 5), and whose orbit comes very close to Mercury's orbit.

Although dust ejected from a comet is subject to additional forces, (radiation pressure, Poytning-Robertson (PR) drag, and gravitational perturbations due to the planets) cometary dust grains will nonetheless tend to remain concentrated in the vicinity of the comet's orbital plane. Dust from Encke will drift radially through its orbit plane due to solar Poynting-Robertson drag (Burns et al., 1979). Encke meteor showers might be expected at Mercury true anomaly ν=46° because this is the longitude where the two planes cross and the orbits are in close proximity (Fig. 6). Encke and the Taurids are believed to be remnants of a much larger comet, which disintegrated over the past 20000 to 30000 years (Whipple, 1940; Klacka, 1999). Planetary gravitational perturbations will drive additional orbital evolution both of the comet and its dust, and that evolution is not strictly coplanar. In particular, planetary perturbations can drive the comet dust out of the comet's orbital plane, which would then allow Mercury to encounter that dust over a broader range of true anomalies. At Earth, Encke contributes several meteor showers that occur at various longitudes that differ by ~20°, including the Taurid meteor showers whose temporal span is 20 - 25 days or about 20 degrees of longitude at Earth. Consequently a shower of Encke dust at Mercury could conceivably occur at ~20 degrees before Mercury has passed through Encke's orbit plane which would then account for the excess exospheric Ca observed at ν=25°±5° in Fig. 1.

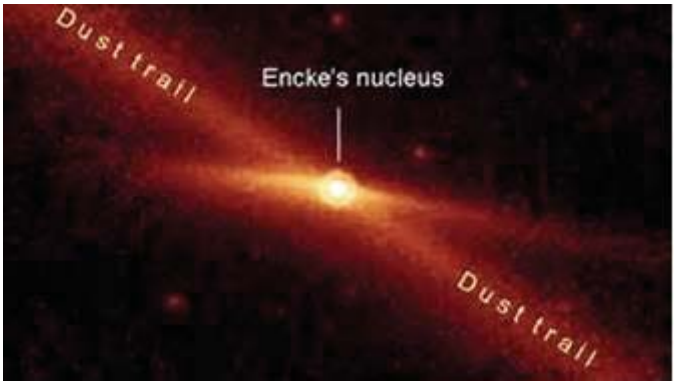

Figure 5. An infrared image from Spitzer Space Telescope obtained 22 July, 2004, shows Comet Encke's nucleus and dust trail (Courtesy NASA/JPL-Caltech and M. Kelley, Univ. of Minnesota).

The orbital parameters of comet 2P/Encke (epoch 2013) are given in Table 2.

Table 2. Orbital Elements for Comet 2P/Encke

Orbital Elements of Comet 2P/Encke (J2000)	
Longitude of Perihelion (deg)	186.53563
Longitude of Ascending Node (deg)	334.57
Inclination (degrees)	11.77897
Eccentricity	0.8482322
Semi-major axis (AU)	2.2147
Period (years)	3.30
Periapse distance (AU)	0.3361267

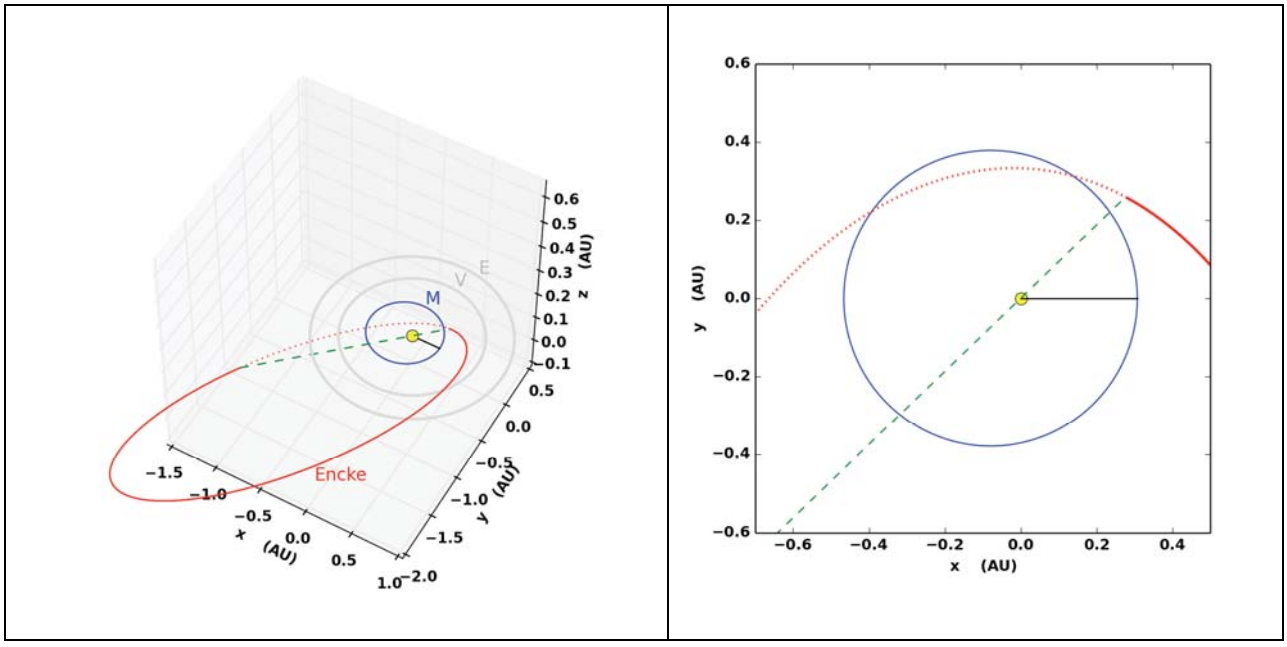

Figure 6. (left) Encke's orbit (red) is shown along with those of Mercury (blue), Venus and Earth (in grey). The coordinate system used here has its x-y plane in Mercury's orbit plane, the direction of the +x axis is towards Mercury's periapsis, and the angles described below are measured counter clockwise from this x-axis. In this coordinate system, Encke's longitude of ascending node is 226° and its descending node is at 46°, and these angles are also Mercury's true anomaly when it crosses Encke's orbit plane. The dashed green line is where these two orbit planes cross. Encke's orbit (red) is projected onto Mercury's orbital plane (the x-y plane) in the right panel. The black line is drawn from the sun (yellow circle) to Mercury's periapse.

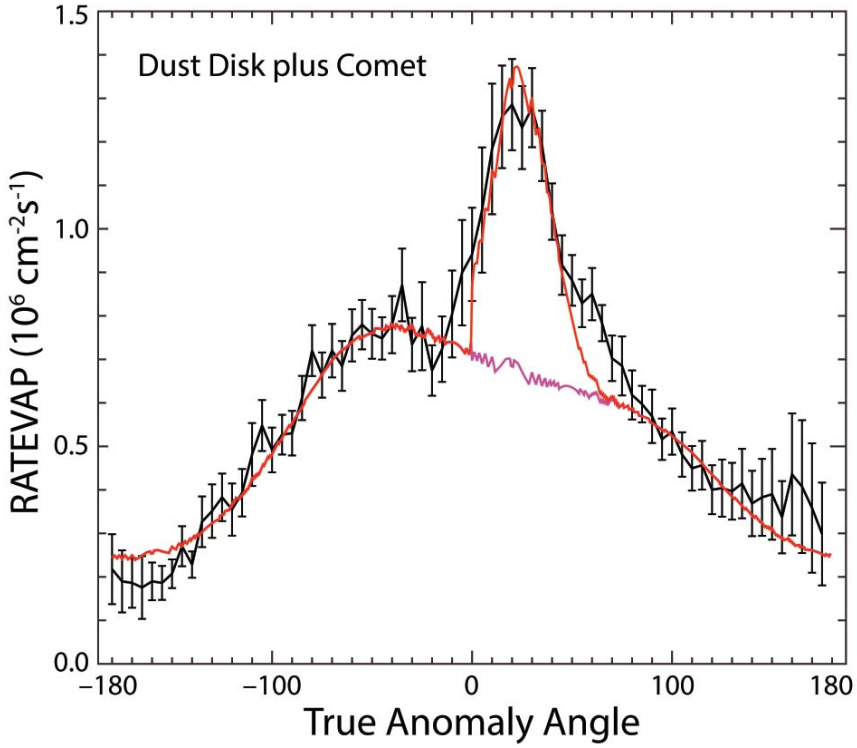

Figure 7. Ca vaporization rate at Mercury due to the interplanetary dust-disk (magenta line) plus a cometary stream whose peak density occurs at true anomaly ν=25°. The Gaussian half-width of the cometary dust stream extends ± 15° when measured in units of Mercury's true anomaly, and the rate is in units of 10^6 atoms cm^{-2} s^{-1}. The red line is the summed contributions from the cometary dust stream plus that due to an interplanetary dust-disk that is inclined 10° from Mercury's orbital plane, and whose ascending node is 290° when measured from Mercury's longitude of perihelion, with the dust density varying as R^{-2}, where R is the heliocentric distance. The MASCS observations are plotted in black. In this model the fraction of Ca-bearing vapor that remains in the uncondensed state when the vapor cloud becomes collisionless is 5.5%.

Figure 7 shows how Mercury's exospheric Ca signal varies with the planet's true anomaly ν when the impacting dust is the sum of two sources: a single circumsolar dust-disk plus that due to a cometary dust stream whose centroid lies at Mercury true anomaly, ν, 25°. Note that MESSENGER MASCS observations constrain the a Gaussian half width of the model's cometary dust stream to about 15° of Mercury's orbital longitude whereas the full width at half-maximum (FWHM) of the Encke dust stream was previously estimated to be 50° at Mercury

(Selsis et al., 2004). Although Mercury passes through Encke's orbit plane twice, the second instance occuring when Mercury's ν=226°, no contribution from the second crossing is included in this model because Encke's and Mercury's orbits are now several astronomical units apart.

To explore how results vary with dust velocity we also performed an additional simulation with impact speeds increased by 15 km/s. Although the higher impact velocity does increase the impact vaporization rate, increased velocity can be offset by reducing the number density of the impacting dust. Because the model's two principal parameters (dust density and dust impact speed) are coupled in this way, this study can only provide plausible estimates rather than firm measurement of both quantities. Nonetheless this uncertainty does not impact our main findings: that the seasonal variations in Mercury's exospheric Ca can be attributed to impacts by interplanetary dust grains plus an additional localized contribution that could be a meteor stream from the nearby comet Encke.

Unlike the meteor streams due to comets Bradfield and Tempel-Tuttle, which impact Mercury at about 70 km/s and at high latitudes, the Encke dust grains impact Mercury with a mean velocity of about 28 km/s and at low latitudes (Christou and Asher, 2009). These velocities are only slightly higher than the mean velocity expected from the dust at Mercury, about 20 km/s (Cintala, 1992). Since all of the MASCS Ca observations analyzed by Burger are from equatorial limb scans, we cannot determine from these data whether there is an effect from those comets that impact at high latitudes.

5. Discussion

5.1 Comparison with earlier work

Kameda et al. (2009) analyzed the possibility that variations in Mercury's sodium exosphere are the result of excursions of Mercury with respect to the interplanetary dust disk. They used data from Mercury's sodium exosphere to derive parameters for a dust distribution based on a least-squares fit to the ν variation of Mercury's exospheric sodium. They assumed a dust density distribution with heliocentric distance, R, and distance from the symmetry plane of the dust-disk, z (assumed to be at an inclination of 2.9 degrees from the ecliptic) with the following functional form:

$$n_{IPD} \propto R^{-\alpha} \exp[-\beta(\frac{z}{R})^2] \quad . \qquad (5)$$

The parameters α, β are free parameters in their model and are fit to the Mercury Na exospheric observations. They also alowed the longitude of the ascending node, Ω_d, and inclination, i, of the dust disk to be free parameters, resulting in i>1.9, and $-104<\Omega_d<57$. Their derived fit is $\beta=50$, $\alpha=0.2$. The Kameda model is therefore a thin flat disk that decreases very little with radial distance from the Sun, but decreases rapidly with latitude.

Our results are consistent with dust models derived from observations of the zodiacal light, HELIOS data or the DIRBE model (Reach, 1991; Leinert et al., 1980; 1976), which conclude that $\alpha \sim 1.5 - 2$. According to Reach (1991) the dust albedo varies as $R^{-0.3}$, not the density.

5.2 Processes imparting additional energy to the atomic calcium

Based on the line-widths and scale heights of the ground-based data, Killen et al. (2005) derived a temperature of the atomic Ca in the range of 12000-20000 K, much higher than the range of temperatures derived from other known species such as Na (1200 K). Killen et al. (2005) suggested that the hot Ca seen in the exosphere is a result of a source consisting of calcium-bearing molecules that are dissociated in the exosphere, thereby obtaining excess energy in the process.

Recently, Burger et al. (2014) derived a temperature for the Ca exosphere in excess of 50000 K using MESSENGER MASCS data. His method was to run a Monte Carlo code with the source's temperature, size, and rate as free parameters to minimize the χ^2 statistic between various assumed source temperatures and do a least squares fit with the model output and data. This method gave a most likely temperature of 70000 K. Mg, also seen in Mercury's exosphere, is similar to Ca in that it has a component of extreme temperature with a source concentrated on the dawn side, although it may also have a lower temperature component, consistent with impact vaporization at 3000 K (Sarantos et al., 2011). Because sodium is a much more volatile element, its source processes are dominated by photon-stimulated desorption (Cassidy et al., 2014), with a characteristic temperature of 1200 K. Temperatures greater than 50000 K cannot be differentiated by scale heights because there is an imperceptible difference between them. What we know is that the atomic Ca is much too hot to be due to

impact vaporization directly. We postulate that the atomic calcium in Mercury's exosphere is the product of Ca-bearing molecules that are ejected in the vapor cloud and subsequently dissociated (Killen et al., 2005). Berezhnoy (2013) assigns Ca-bearing impact products as a function of quenching temperature, along with photo-dissociation reactions, the probability of dissociation at the Moon on a single trajectory at 3000 K, and excess energy of photolysis (see Table 4). Photodissociation may not be the process acting at Mercury, but we give these rates as a guideline.

Table 4. Ca-bearing molecules, dissociation pathways, probability of photodissociation on one trajectory at 3000 K at the Moon (P_{phot}), and excess energy of dissociation (E_{phot}) (from Berezhnoy, 2013).

Initial Product	Dissociation path	P_{phot}	E_{phot} (eV)
$Ca(OH)_2$	$Ca(OH)_2+h\nu=CaOH+OH$	0.5	0.6
CaOH	$CaOH+h\nu=Ca+OH$	1.0	0.6
CaOH	$CaOH+h\nu=CaO+H$	0.9	0.04
CaO	$CaO+h\nu=Ca+O$	1.0	0.6

At Mercury, with a solar flux rate 4.6 - 10.6 times that at the Earth/Moon system, the most likely product of impact vaporization, $Ca(OH)_2$, (Berezhnoy, 2013), is virtually certain to dissociate to Ca without returning to the surface. If the initial temperature of the fireball is 3500 K, the initial energy of the products is about 0.3 eV. Either of the pathways for destruction of $Ca(OH)_2$, the most probable product at quenching, would result in a gain of about 1.2 eV, resulting in a neutral Ca product with about 1.5 eV of energy. Taken at thermodynamic equilibrium, the Ca would have a temperature of about 17500 K, consistent with the temperature derived from line widths. In fact, given that the Ca at 1.5 eV is escaping from Mercury, and each atom subsequently encounters lower gravity as the altitude above the surface increases, and in addition is accelerated by radiation pressure, the apparent scale height would increase naturally with altitude (e.g. Cassidy et al., 2014). Therefore the temperature of 70000 K derived from the Monte Carlo code of Burger et al. (2014) may result from rapidly decreasing gravity and radiation pressure and not from an initial 3 eV of energy. However, additional energy beyond that provided by dissociation may be gained by recombination following ionization.

5.3 Fraction of Impact-Ejected calcium in the extreme temperature regime

538 The average fraction of Ca in Mercury's surface is 5.9 wt% (Evans et al., 2012). Given an
539 average weight of all elements of 24.4, the Ca fraction by number is 3.54%. According to
540 Berezhnoy et al. (2011) the ratio of Ca in the gas phase to Ca in all phases in the exosphere is ~
541 0.05. Our code gives the total gas phase, including molecules. For our code, the fraction of all Ca
542 vaporized in our models that is required to fit the measured atomic Ca varies from 2 - 12%
543 depending on the model. Our best-fit model (Figure 7) has a fraction of vaporized Ca in the
544 uncondensed state of 5.5%, consistent with the Berezhnoy number.
545
546 As a first order check on our model, we multiplied the total rate of gas plus melt calculated by
547 Cintala (1992) by the fraction of Ca in the regolith, and then by 0.05 (the assumed fraction of Ca
548 in the gas phase) to compare with the observed Ca abundance in the exosphere. Using the Ca
549 photoionization lifetime from Huebner and Mukerjee (2011) of 1.4×10^4 sec at Earth, (1311 s at
550 Mercury perihelion or 3027 s at aphelion) we derived an approximate zenith column abundance
551 of Ca of 6.9×10^8 cm^{-2} at perihelion, which agrees within a factor of two with the observed
552 tangent column at dawn of about 2×10^9 cm^{-2} (Burger et al., 2014). Note that at the extreme
553 temperature derived for the Ca exosphere, the ratio of the tangent column at the surface to the
554 zenith column is only about 1.25 (See Chamberlain and Hunten, 1987, eqn. 7.1.63).
555
556 **6. Conclusions**
557
558 The seasonal variations in Mercury's calcium exosphere can be partially explained as being
559 due to Mercury's radial and vertical motions through an interplanetary dust disk that is
560 more concentrated sunwards and tipped less than 10 degrees away from Mercury's orbital
561 plane. The best fit is tipped less than 5° from Mercury's orbital plane. Mercury's
562 heliocentric distance varies from 0.306 AU at perihelion to 0.465 AU at aphelion, and the
563 variations in the exospheric Ca source rate do follow the behavior that is expected from
564 impact vaporization by interplanetary dust, with the observed seasonal variations largely
565 due to Mercury's substantial radial excursions through the interplanetary dust-disk.
566 However, a notable exception is a persistent enhancement seen in the calcium exosphere
567 when Mercury's true anomaly is near 25°± 5°. An enhancement in the impact vaporization
568 rate near perihelion is attributed to excursion of Mercury through the plane of a dust disk
569 that increases in density sunward but the peak after perihelion is more problematic.
570 However, impact vaporization due to a single dust disk cannot explain all the variations seen in
571 Mercury's Ca source rate; the strong peak in the Ca signal near ν=25°±5° requires an additional
572 source of dust (see Fig. 1). We did consider whether the enhanced Ca signal at ν=25°±5° might
573 be due to a secondary dust disk (which itself could for instance be due to a very dusty cometary

outburst or disintegration occurring in the recent past) that might be tilted with respect to the main dust-disk's mid-plane. Although we could obtain marginally satisfactory fits to the Ca observations using this two-disk model, the results were inconsistent with other observations of inner zodiacal light (Reach, 1991; Leinert et al., 1980; 1976; Hahn et al., 2002). If the Ca excess were in fact caused by Mercury's orbit carrying it through the midplane of such a tilted dust-disk, then a another smaller but still detectable enhancement in exospheric Ca should occur when Mercury passes through the dust-disk's midplane a second time 180 degrees later in its orbit. The absence of an observed secondary enhancement in Ca at true anomaly 25°±5° degrees after aphelion limits the inclination of the primary interplanetary dust disk to less than 10°. The MESSENGER MASCS observations of exospheric Ca are best fit by an interplanetary dust-disk whose density varies radially as $R^{-1.45}$ to R^{-2} (Figures 3, 4 and 7) consistent with the Hahn et al. (2002) model for dust in the inner Solar System.

We also show that the enhancement in Ca 25°±5° degrees after perihelion can be attributed to the crossing of Mercury's orbital plane and a comet stream. A likely candidate is comet 2P/Encke, even though the enhancement occurs ~25° before Mercury crosses the comet's orbital plane. However this discrepancy is not problematic since Encke also produces several meteor showers at Earth that are spatially segregated in longitude by about 20° - 30° around Earth's orbit (Klacka, 1999). Our model estimates that 2 - 10% of the initially vaporized calcium remains in the form of hot uncondensed Ca, bracketing the Berezhnoy (2010; 2013) estimate that globally 5% of the calcium-bearing vapor remains in the atomic uncondensed state. In our model this fraction depends on the assumed radial dependence of interplanetary dust, which governs the dust density at Mercury's orbit.

Acknowledgments. RMK was supported by NASA grant NNX07AR78G-S01 as a Participating Scientist on the NASA MESSENGER mission to Mercury, and by STROFIO, a NASA Mission of Opportunity on the Bepi-Colombo mission. JMH's efforts here were supported by the National Science Foundation via Grant No. AST-1313013. JMH thanks Byron Tapley for graciously providing office space and the use of the facilities at the University of Texas Center for Space Research (CSR). We thank Dr. Apostolos Christou for many helpful conversations concerning cometary dust and Dr. Matthew Burger for discussions concerning the MASCS Ca data.

References

609 Berezhnoy, A.A., 2013. Chemistry of impact events on the Moon, *Icarus* 226, 205-211,
610 doi:/10.1016/j.icarus.2013.05.030.
611 Berezhnoy, A.A., 2010. Meteoroid bombardment as a source of the lunar exosphere. *Adv. Space*
612 *Res.* 45, 70 - 76.
613 Berezhnoy, A.A., V. Mangano, A. Mura, A. Milillo, and S. Orsini, 2011. Density distribution of
614 metal-containing species in the exosphere of Mercury after meteoroids impacts. EPSC-DPS
615 Joint Meeting 2011, Vol. 6, EPSC-DPS2011-1793.
616 Berezhnoy, A.A. and B.A. Klumov, 2008. Impacts as sources of the exosphere on Mercury.
617 *Icarus* 195, 511-522. doi:10.1016/j.icarus.2008.01.005.
618 Bida, T.A., R.M. Killen, and T.H. Morgan 2000. Discovery of Ca in the atmosphere of Mercury.
619 *Nature*, 404, 159-161.
620 Borin, P., G. Cremonese, F. Marzari, M. Bruno, and S. Marchi, 2009. Statistical analysis of
621 micrometeoroids flux on Mercury *Astron. Astrophys.* 503, 259–264. DOI: 10.1051/0004-
622 6361/200912080.
623 Burger, M. H., R.M. Killen, W.E. McClintock, A.W. Merkel, R.J. Vervack, Jr., T.A. Cassidy,
624 and M. Sarantos, 2014. Seasonal Variations in Mercury's Dayside Calcium Exosphere.
625 *Icarus,* DOI: 10.1016/j.icarus.2014.04.049.
626 Burger, M. H., R.M. Killen, W.E. McClintock, R.J. Vervack, Jr., A.W. Merkel, A.L. Sprague,
627 and M. Sarantos, 2012. Modeling MESSENGER Observations of Calcium in Mercury's
628 Exosphere. *Journ. Geophys. Res*. 117, 0L11B, doi:10.1029/2012JE004158.
629 Burns, J. A., P.L. Lamy, and S. Soter, 1979. Radiation forces on small particles in the solar
630 system. Icarus 40, 1-48, doi:10.1016/0019-1035(79)90050-2.
631 Cassidy, T.A. and R.E. Johnson, 2005. Monte Carlo model of sputtering and other ejection
632 processes within a regolith. *Icarus* 176, 499-507, doi:10.1016/j.icarus.2005.02.013
633 Cassidy, Timothy A., Aimee W. Merkel, Matthew H. Burger, Rosemary M. Killen, William E.
634 McClintock, Ronald J. Vervack, Jr., Menelaos Sarantos, 2014. Mercury's Seasonal Sodium
635 Exosphere: MESSENGER Observations from Mercury Orbit, *Icarus*,
636 10.1016/j.icarus.2014.10.037.
637 Chamberlain, J.W. and D.M. Hunten, 1987. *Theory of Planetary Atmospheres*, 2nd Ed.,
638 Academic Press, Orlando.
639 Christou, A and D. Asher, 2009. Possible Meteoroid streams at Mercury. *Hermean Exospheres*
640 *Workshop*, Graz, Austria, 12-13 November, 2009.
641 Cintala, M.J., 1992. Impact-Induced Thermal Effects in the Lunar and Mercurian Regoliths.
642 *Journ. Geophys. Res.* 97, 947-973.
643 Collette, A., Z. Sternovsky, and M. Horanyi, 2014. Production of neutral gas by micrometeoroid
644 impacts. *Icarus* 227, 89-93, doi: 10.1016/j.icarus.2013.09.009.

645 Evans, L. G., P.N. Peplowski, E.A. Rhodes, D.J. Lawrence, +10 co-authors, 2012. Major-
646 element abundances on the surface of Mercury: Results from the MESSENGER Gamma-
647 Ray Spectrometer, *J. Geophys. Res.*, 117, E00L07, doi:10.1029/2012JE004178.
648 Fentzke, J.T. and D. Janches, 2008. A semi-empirical model of the contribution from sporadic
649 meteoroid sources on the meteor input function in the MLT observed at Arecibo. *Journ.*
650 *Geophys. Res.*, 113, A03304, doi:10.1029/2007JA012531.
651 Hahn, J.M., H.A. Zook, B. Cooper, and B. Sunkara. 2002. Clementine Observations of the
652 Zodiacal Light and the Dust Content of the Inner Solar System. *Icarus* 158, 360-378.
653 Huebner, W.F., and J. Mukherjee, Photo Rate Coefficient Database, 2011.
654 http://phidrates.space.swri.edu.
655 Janches, Diego, Craig J. Heinselman, Jorge L. Chau, Amal Chandran, and Ronald Woodman,
656 2006. Modeling the global micrometeor input function in the upper atmosphere observed by
657 high power and large aperture radars *Journ. Geophys. Res.*, 111, A07317,
658 doi:10.1029/2006JA011628.
659 Kameda, S., I. Yoshikawa, M. Kagitani, and S. Okano, 2009. Interplanetary dust distribution and
660 temporal variability of Mercury's atmospheric Na. *Geophys. Res. Lett.* 36, L15201,
661 doi:10.1029/2009GL039036.
662 Killen, R.M., T.A. Bida, and T.H. Morgan, 2005. The calcium exosphere of Mercury, *Icarus*,
663 173#2, 300-311.
664 Klačka, Jozef. 1999. Meteor Streams of Comet Encke. Taurid Meteor Complex. arXiv:astro-
665 ph/9910045.
666 Lange, M.A. and T.J. Ahrens, 1982. The evolution of an impact generated atmosphere. *Icarus*
667 51, 96-120.
668 Leinert, C., E. Pitz, H. Link, M. Hanner, E. Grun, H. Fechtig, J. Kissel, and P. Gammelin. 1976.
669 Preliminary Results of the Helios A Zodiacal Light and Micrometeoroid Experiments. *Bull.*
670 *Am. Ast. Soc.*, 8, 457.
671 Leinert, C., M. Hanner, I. Richter and E. Pitz. 1980. The Plane of Symmetry of Interplanetary
672 Dust in the Inner Solar System. *Astron. Astrophys*. 82, 328-336.
673 Love, S.G. and D.E. Brownlee, 1993. A Direct Measurement of the Terrestrial Mass Accretion
674 Rate of Cosmic Dust. *Science* 262, 550-553.
675 McClintock, W.E. and M.R. Lankton. 2007. The Mercury Atmospheric and Surface Composition
676 Spectrometer for the MESSENGER Mission. *Space Science Reviews* 131, 481-521,
677 doi:10.1007/s11214-007-9264-5.
678 Marchi, S., A. Morbidelli, and G. Cremonese, 2005. Flux of meteoroid impacts on Mercury,
679 *Astron. Astrophys.* 431, 1123-1127. DOI: 10.1051/0004-6361:20041800 .
680 Melosh, H.J., 1989. *Impact Cratering a Geologic Process.* Oxford Univ. Press, Oxford.

681 Misconi, N.Y. and J.L. Weinberg, 1978, Is Venus concentrating interplanetary dust toward its
682 orbital plane *Science* 200, 1484.
683 Morgan, T.H. and R.M. Killen, 1998. Production mechanisms for faint but possibly detectable
684 coronae about asteroids. *Planet. Space Sci.* 46, 843-850.
685 O'Keefe, J.D. and T.J. Ahrens. 1977. Impact induced energy partitioning, melting, and
686 vaporization on terrestrial planets. *Proc. Lunar Sci. Conf.* 8th 3357-3374.
687 Reach, W.T., 1991. Zodiacal Emission II. Dust near the ecliptic. *Astrophys. Journ*. 369, 529-543.
688 Sarantos, M., Rosemary M. Killen, William E. McClintock, E. Todd Bradley, Ronald J. Vervack
689 Jr., Mehdi Benna, James A. Slavin, Limits to Mercury's magnesium exosphere from
690 MESSENGER second flyby observations ,*Planetary and Space Science* 59 #15, 1992-2003,
691 doi: 10.1016/j.pss.2011.05.002.
692 Selsis, F., Brillet, J., Rapaport, M., 2004. Meteor showers of cometary origin in the Solar
693 System: Revised predictions. *Astronomy and Astrophysics*, 416, 783-789.
694 Whipple, F.L. 1940. Photographic meteor studies. III. The Taurid shower, *Proceedings of the*
695 *American Philosophical Society* 83, 711- 745.